Surface plasmon-enhanced nanoscopy of intracellular cytoskeletal actin filaments using random nanodot arrays

Youngjin Oh,[1,5] Taehwang Son,[1,5] Sook Young Kim,[2] Wonju Lee,[1] Heejin Yang,[1] Jong-ryul Choi,[3] Jeon-Soo Shin,[2,4] and Donghyun Kim[1]*

[1] *School of Electrical and Electronic Engineering, Yonsei University, Seoul, 120–749, South Korea*
[2] *Department of Microbiology, Yonsei University College of Medicine, Seoul, 120–752, South Korea*
[3] *Medical Device Development Center, Daegu-Gyeongbuk Medical Innovation Foundation, Daegu, 701-310, South Korea*
[4] *BK21 PLUS for Medical Science, Yonsei University College of Medicine, Seoul, 120–752, South Korea*
[5] *These authors contributed equally to this work.*
kimd@yonsei.ac.kr

Abstract: The feasibility of super-resolution microscopy has been investigated based on random localization of surface plasmon using blocked random nanodot arrays. The resolution is mainly determined by the size of localized fields in the range of 100-150 nm. The concept was validated by imaging FITC-conjugated phalloidin that binds to cellular actin filaments. The experimental results confirm improved resolution in reconstructed images. Effect of far-field registration on image reconstruction was also analyzed. Correlation between reconstructed images was maintained to be above 81% after registration. Nanodot arrays are synthesized by temperature-annealing without sophisticated lithography and thus can be mass-produced in an extremely large substrate. The results suggest a super-resolution imaging technique that can be accessible and available in large amounts.

OCIS codes: (100.6640) Superresolution; (180.2520) Fluorescence microscopy; (250.5403) Plasmonics; (280.1415) Biological sensing and sensors; (310.6628) Subwavelength structures, nanostructures.

References and links

1. E. Betzig, G. H. Patterson, R. Sougrat, O. W. Lindwasser, S. Olenych, J. S. Bonifacino, M. W. Davidson, J. Lippincott-Schwartz, and H. F. Hess, "Imaging intracellular fluorescent proteins at nanometer resolution," Science **313**(5793), 1642–1645 (2006).
2. M. J. Rust, M. Bates, and X. Zhuang, "Sub-diffraction-limit imaging by stochastic optical reconstruction microscopy (STORM)," Nat. Methods **3**(10), 793–796 (2006).
3. S. W. Hell, "Far-field optical nanoscopy," Science **316**(5828), 1153–1158 (2007).
4. D. Yelin, D. Oron, S. Thiberge, E. Moses, and Y. Silberberg, "Multiphoton plasmon-resonance microscopy," Opt. Express **11**(12), 1385–1391 (2003).
5. H. Szmacinski, V. Toshchakov, W. Piao, and J. R. Lakowicz, "Imaging of protein secretion from a single cell using plasmonic substrates," Bionanoscience **3**(1), 30–36 (2013).
6. K.-F. Giebel, C. Bechinger, S. Herminghaus, M. Riedel, P. Leiderer, U. Weiland, and M. Bastmeyer, "Imaging of cell/substrate contacts of living cells with surface plasmon resonance microscopy," Biophys. J. **76**(1), 509–516 (1999).
7. M. R. Gartia, A. Hsiao, M. Sivaguru, Y. Chen, and G. L. Liu, "Enhanced 3D fluorescence live cell imaging on nanoplasmonic substrate," Nanotechnology **22**(36), 365203 (2011).
8. R.-Y. He, C.-Y. Lin, Y.-D. Su, K.-C. Chiu, N.-S. Chang, H.-L. Wu, and S.-J. Chen, "Imaging live cell membranes via surface plasmon-enhanced fluorescence and phase microscopy," Opt. Express **18**(4), 3649–3659 (2010).
9. J. Kottmann, O. Martin, D. Smith, and S. Schultz, "Spectral response of plasmon resonant nanoparticles with a non-regular shape," Opt. Express **6**(11), 213–219 (2000).
10. E. X. Jin and X. Xu, "Obtaining super resolution light spot using surface plasmon assisted sharp ridge nanoaperture," Appl. Phys. Lett. **86**(11), 111106 (2005).
11. W. Lee, K. Kim, and D. Kim, "Electromagnetic near-field nanoantennas for subdiffraction-limited surface plasmon-enhanced light microscopy," IEEE J. Sel. Top. Quant. **18**(6), 1684–1691 (2012).

#221980 - $15.00 USD Received 1 Sep 2014; revised 25 Oct 2014; accepted 25 Oct 2014; published 31 Oct 2014

12. S. Gresillon, L. Aigouy, A. C. Boccara, J. C. Rivoal, X. Quelin, C. Desmarest, P. Gadenne, V. A. Shubin, A. K. Sarychev, and V. M. Shalaev, "Experimental observation of localized optical excitations in random metal-dielectric films," Phys. Rev. Lett. **82**(22), 4520–4523 (1999).
13. H. Cang, A. Labno, C. Lu, X. Yin, M. Liu, C. Gladden, Y. Liu, and X. Zhang, "Probing the electromagnetic field of a 15-nanometre hotspot by single molecule imaging," Nature **469**(7330), 385–388 (2011).
14. K. Kim, J. Yajima, Y. Oh, W. Lee, S. Oowada, T. Nishizaka, and D. Kim, "Nanoscale localization sampling based on nanoantenna arrays for super-resolution imaging of fluorescent monomers on sliding microtubules," Small **8**(6), 892–900 (2012).
15. J. Choi, K. Kim, Y. Oh, A. L. Kim, S. Y. Kim, J.-S. Shin, and D. Kim, "Extraordinary transmission-based plasmonic nanoarrays for axially super-resolved cell imaging," Adv. Opt. Mater. **2**(1), 48–55 (2014).
16. K. Kim, Y. Oh, W. Lee, and D. Kim, "Plasmonics-based spatially activated light microscopy for super-resolution imaging of molecular fluorescence," Opt. Lett. **35**(20), 3501–3503 (2010).
17. T. Lohmüller, S. Triffo, G. P. O'Donoghue, Q. Xu, M. P. Coyle, and J. T. Groves, "Supported membranes embedded with fixed arrays of gold nanoparticles," Nano Lett. **11**(11), 4912–4918 (2011).
18. K. Kim, J. W. Choi, K. Ma, R. Lee, K. H. Yoo, C. O. Yun, and D. Kim, "Nanoisland-based random activation of fluorescence for visualizing endocytotic internalization of adenovirus," Small **6**(12), 1293–1299 (2010).
19. D. M. Yeh, C. F. Huang, C. Y. Chen, Y. C. Lu, and C. C. Yang, "Localized surface plasmon-induced emission enhancement of a green light-emitting diode," Nanotechnology **19**(34), 345201 (2008).
20. Y. Wang, M. Becker, L. Wang, J. Liu, R. Scholz, J. Peng, U. Gösele, S. Christiansen, D. H. Kim, and M. Steinhart, "Nanostructured gold films for SERS by block copolymer-templated galvanic displacement reactions," Nano Lett. **9**(6), 2384–2389 (2009).
21. E. Le Moal, S. Lévêque-Fort, M.-C. Potier, and E. Fort, "Nanoroughened plasmonic films for enhanced biosensing detection," Nanotechnology **20**(22), 225502 (2009).
22. W. Yuan, H. P. Ho, R. K. Y. Lee, and S. K. Kong, "Surface-enhanced Raman scattering biosensor for DNA detection on nanoparticle island substrates," Appl. Opt. **48**(22), 4329–4337 (2009).
23. E. Giorgetti, S. Cicchi, M. Muniz-Miranda, G. Margheri, T. Del Rosso, A. Giusti, A. Rindi, G. Ghini, S. Sottini, A. Marcelli, and P. Foggi, "Förster resonance energy transfer (FRET) with a donor-acceptor system adsorbed on silver or gold nanoisland films," Phys. Chem. Chem. Phys. **11**(42), 9798–9803 (2009).
24. A. Urich, A. Pospischil, M. M. Furchi, D. Dietze, K. Unterrainer, and T. Mueller, "Silver nanoisland enhanced Raman interaction in grapheme," Appl. Phys. Lett. **101**(15), 153113 (2012).
25. Y. H. Jang, K. Chung, L. N. Quan, B. Špačková, H. Šípová, S. Moon, W. J. Cho, H. Y. Shin, Y. J. Jang, J. E. Lee, S. T. Kochuveedu, M. J. Yoon, J. Kim, S. Yoon, J. K. Kim, D. Kim, J. Homola, and D. H. Kim, "Configuration-controlled Au nanocluster arrays on inverse micelle nano-patterns: versatile platforms for SERS and SPR sensors," Nanoscale **5**(24), 12261–12271 (2013).
26. H. Yu, K. Kim, K. Ma, W. Lee, J. W. Choi, C. O. Yun, and D. Kim, "Enhanced detection of virus particles by nanoisland-based localized surface plasmon resonance," Biosens. Bioelectron. **41**(15), 249–255 (2013).
27. S. H. Lim, D. Derkacs, and E. T. Yu, "Light scattering into silicon-on-insulator waveguide modes by random and periodic gold nanodot arrays," J. Appl. Phys. **105**(7), 073101 (2009).
28. S.-P. Ng, X. Q. Lu, N. Ding, C.-M. L. Wu, and C.-S. Lee, "Plasmonic enhanced dye-sensitized solar cells with self-assembly gold-TiO2@core–shell nanoislands," Sol. Energy **99**, 115–125 (2014).
29. A. B. Dahlin, J. O. Tegenfeldt, and F. Höök, "Improving the instrumental resolution of sensors based on localized surface plasmon resonance," Anal. Chem. **78**(13), 4416–4423 (2006).
30. D. Gao, W. Chen, A. Mulchandani, and J. S. Schultz, "Detection of tumor markers based on extinction spectra of visible light passing through gold nanoholes," Appl. Phys. Lett. **90**(7), 073901 (2007).
31. J. A. Barden, M. Miki, B. D. Hambly, and C. G. Dos Remedios, "Localization of the phalloidin and nucleotide-binding sites on actin," Eur. J. Biochem. **162**(3), 583–588 (1987).
32. J. A. Cooper, "Effects of cytochalasin and phalloidin on actin," J. Cell Biol. **105**(4), 1473–1478 (1987).
33. L. Blanchoin, K. J. Amann, H. N. Higgs, J. -B. Marchand, D. A. Kaiser, and T. D. Pollard, "Direct observation of dendritic actin filament networks nucleated by Arp2/3 complex and WASP/Scar proteins," Nature **404**(6781), 1007–1011 (2000).
34. Y. Kanamori, K. Hane, H. Sai, and H. Yugami, "100 nm period silicon antireflection structures fabricated using a porous alumina membrane mask," Appl. Phys. Lett. **78**(2), 142–143 (2001).
35. J. Cesario, R. Quidant, G. Badenes, and S. Enoch, "Electromagnetic coupling between a metal nanoparticle grating and a metallic surface," Opt. Lett. **30**(24), 3404–3406 (2005).
36. K. M. Byun, S. J. Yoon, D. Kim, and S. J. Kim, "Experimental study of sensitivity enhancement in surface plasmon resonance biosensors by use of periodic metallic nanowires," Opt. Lett. **32**(13), 1902–1904 (2007).
37. K. Kandere-Grzybowska, C. Campbell, Y. Komarova, B. A. Grzybowski, and G. G. Borisy, "Molecular dynamics imaging in micropatterned living cells," Nat. Methods **2**(10), 739–741 (2005).
38. S. Szunerits, V. G. Praig, M. Manesse, and R. Boukherroub, "Gold island films on indium tin oxide for localized surface plasmon sensing," Nanotechnology **19**(19), 195712 (2008).
39. J. B. Sibarita, "Deconvolution microscopy," Adv. Biochem. Eng. Biotechnol. **95**, 201–243 (2005).
40. C. Preza, M. I. Miller, L. J. Thomas, Jr., and J. G. McNally, "Regularized linear method for reconstruction of three-dimensional microscopic objects from optical sections," J. Opt. Soc. Am. A **9**(2), 219–228 (1992).

#221980 - $15.00 USD Received 1 Sep 2014; revised 25 Oct 2014; accepted 25 Oct 2014; published 31 Oct 2014

1. Introduction

Imaging techniques to achieve super-resolution below the diffraction limit have drawn tremendous interests to understand the molecular nature of macroscopic phenomena. Many different techniques have been developed, such as PALM, STORM, and STED microscopy under total internal reflection fluorescence (TIRF) to achieve subdiffraction-limited resolution [1–3]. Conventional fluorescence microscopy has also been combined with prior information on molecular characteristics to attain super-resolution [4]. Recently, labeled and non-labeled imaging techniques emerge based on the excitation of surface plasmon (SP) formed at the interface between dielectric and metal thin film layers [5–8]. Subdiffraction-limited microscopy techniques have also been attempted, which rely on the localized near-fields due to SP localization in the presence of metallic subwavelength structures at vertices smaller than light wavelength [9]. Near-fields can thereby be localized to a hot spot that is spatially smaller than the diffraction limit [10,11], which was experimentally confirmed [12,13]. SP-enhanced near-field localization has been applied to molecular imaging. For example, periodic nanohole arrays were used to image gliding microtubules and membrane proteins [14,15]. Switching of light incidence was utilized to switch localized fields where image resolution was basically determined by the feature size of nanostructures [16]. Fabrication of periodic nanostructures is often difficult and limited due to the use of low-throughput lithographic processes.

For this reason, nanopatterns such as nanoparticles or nanoislands were synthesized and arranged in a pseudorandom array for improved image resolution [17,18]. Advantages of the random nanopatterns are clear: they are easy to synthesize and sophisticated fabrication equipment is not required. Therefore, use of random nanopatterns has far exceeded imaging applications, such as in the enhancement of optical signals in light-emitting diodes [19], biosensors [20–26], photodetectors [27] and solar cells [28]. Also, nanoholes in a random configuration were used as detection substrates based on light extinction [29,30].

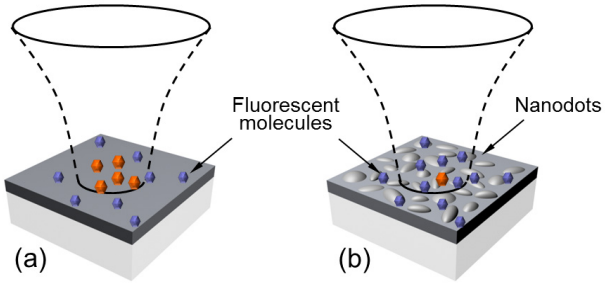

Fig. 1. Schematic illustration of SP-enhanced randomly activated (SUPRA) microscopy. In conventional microscopy in (a), fluorescent molecules (shown in orange) are excited within a field-of-view. In contrast, SUPRA microscopy in (b) has target fluorescence excited by the field that is localized by nanodot arrays within a field-of-view.

Despite the simplicity of the sample preparation, however, use of random nanopatterns suffers from the difficulty in obtaining super-resolved images because the randomness in the patterns and the near-field that arises almost prohibits deconvolution for image reconstruction. In this paper, we investigate SP-enhanced randomly activated (SUPRA) microscopy based on aligned blocks of temperature-controlled random nanodot arrays to produce super-resolved images by performing image deconvolution and yet retaining the simplicity of nanosynthesis. Target fluorescence emitted by the dyes that are specifically bound to target molecules is excited by the field localized at the nanodot arrays, as shown in the schematic illustrated in Fig. 1. While the point-spread function (PSF) of far-field optics does not change, PSF is reduced effectively due to the localization by the nanodot arrays to be much smaller than the diffraction limit. Super-resolved images can be obtained by acquisition with far-field optics and reconstruction. Although we focus on mass-producible random

#221980 - $15.00 USD Received 1 Sep 2014; revised 25 Oct 2014; accepted 25 Oct 2014; published 31 Oct 2014

nanodots here, we emphasize that the approach is not specific to nanodot patterns, but can be extended to imaging techniques based on arbitrary nanostructures for the excitation of near-fields and the image acquisition in the far-field. Also, SUPRA microscopy can be extremely powerful from a commercial perspective, as it allows a simple optical microscope to be transformed into one with super-resolution if an image is acquired on a nanopatterned surface and more importantly the resolution can be achieved on demand, depending on the pattern. Note that SUPRA microscopy in principle requires perfect registration between near-field distribution created by synthesized pseudorandom nanopatterns and acquired far-field images. The registration is enabled by synthesizing random patterns in pre-aligned blocks which can be matched and aligned in the far field. In this study, the concept of SUPRA microscopy was validated by imaging the distribution of phalloidin in a cell cultured, which binds filamentous actin (F-actin) and is thus highly useful for localizing actin filaments and visualizing their distribution in cells with light microscopy [31–33].

2. Materials and methods

2.1 Synthesis of random Nanodot arrays

For the preparation of aligned nanodot blocks, a 2-nm thick chrome adhesion layer and a silver film were deposited on BK7 glass substrate. Another layer of chrome was then evaporated to prevent the underlying silver from being annealed. After polymethyl methacrylate resist (Allresist, Strausberg, Germany) was spin-coated at 8000 rpm to produce a 150-nm thick layer on the silver film, a square block of 12.2 × 12.2 μm^2 in size was lithographically defined in an overall area of 1 × 1 mm^2 and developed. This is followed by the deposition of a 10~20-nm thick silver film, which is temperature-annealed in a baking oven under high temperature (200°C) for 5 min and is transformed into nanodots. Lift-off of silver was then performed by removing the resist layer.

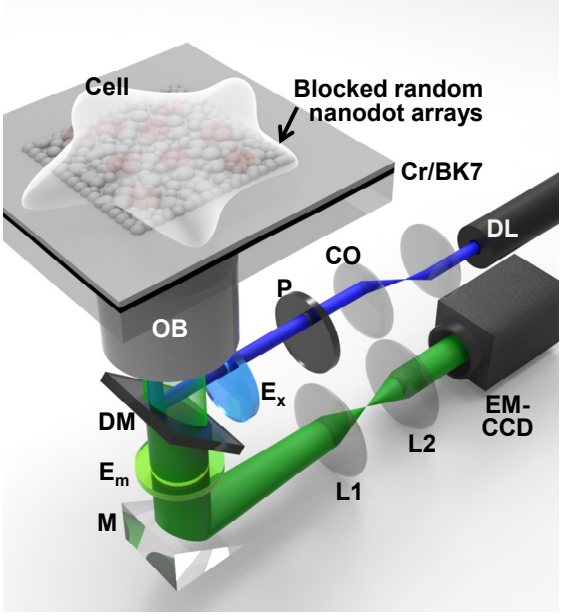

Fig. 2. Illustration of the optical set-up used for SUPRA microscopy (OB.: objective lens (60x, NA 1.49), DL: diode laser, CO: beam expanding collimator, P: polarizer, Ex: excitation fluorescence filter, DM: dichroic mirror, Em: emission filter, M: mirror, L: relay lenses, EM-CCD: EM-CCD camera). The illustration also shows a cell on the nanodot array sample.

#221980 - $15.00 USD Received 1 Sep 2014; revised 25 Oct 2014; accepted 25 Oct 2014; published 31 Oct 2014

2.2 Numerical calculation of near-fields

To understand the effects of geometrical parameters of nanodot arrays, we have calculated the near-field distribution using rigorous coupled-wave analysis (RCWA). RCWA has been used successfully to calculate optical characteristics of various nanostructures [34–36]. For the calculation, 40 × 40 spatial harmonic orders were employed with TM polarized light incidence at $\theta = 60°$ and $\lambda = 488$ nm. For accurate calculation of nanodot array patterns, a SEM image of a nanodot array sample was transferred into a binary mask with a unit size of a single pixel at 48 nm.

2.3 Optical set-up

The main data were measured by a laser TIRFM system (Eclipse TE2000-E, Nikon, Japan). The optical set-up illustrated in Fig. 2 employs a diode laser ($\lambda = 488$ nm, 20 mW, Sapphire 488-20, Coherent, Santa Clara, CA, USA) as light source. The incident light passes through a polarizer (ratio 100:1), which consists of polarization maintaining fiber patch cords and connectors, on an oil-immersion objective lens (CFI Apochromat TIRF 60x, NA = 1.49, Nikon) that interfaces a cover-glass dish substrate, where silver nanodot array substrates are mounted. Light incidence at the interface was estimated at 60° and maintained throughout the experiments. Fluorescence images were acquired by an electron-multiplying charge coupled device (EM-CCD) camera (C9100-12, Hamamatsu, Japan) through a bandpass filter (#74400, EX 450-490, DM 505, BA 520, Chroma, Rockingham, VT, USA).

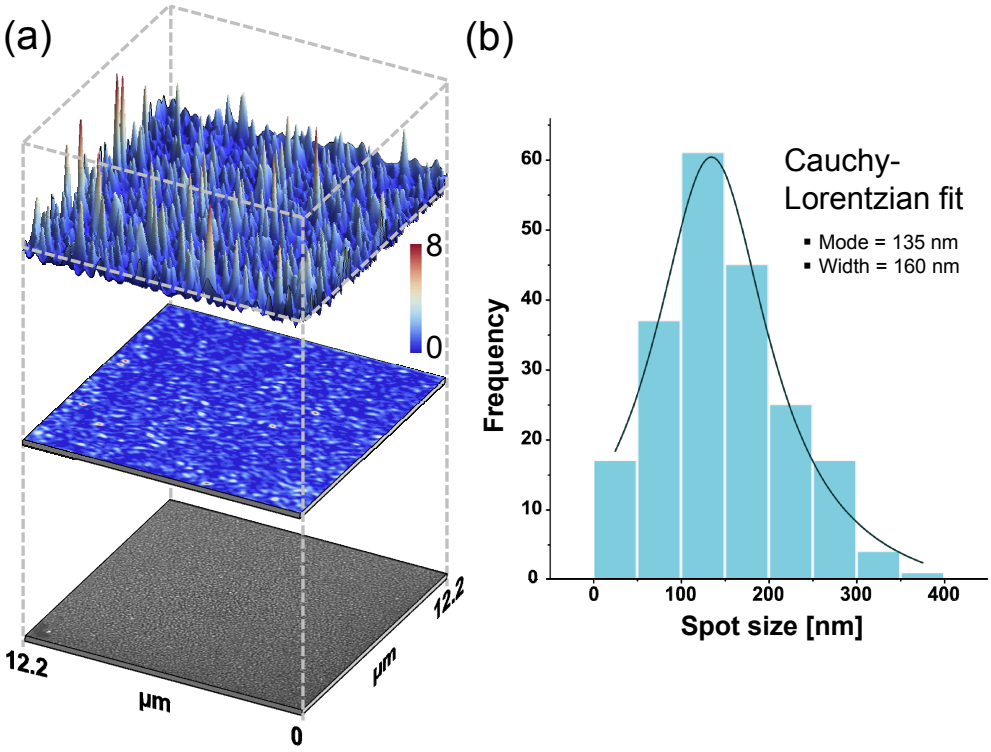

Fig. 3. (a) 3D and 2D near-field intensity ($|E|^2$) distribution overlayed with a nanodot array pattern of Fig. 1. (b) Histogram of spot size from size analyses performed for the near-field data. The results show that the size is the most likely to fall in the range of 100 – 150 nm in terms of modes. The histogram is fitted well with a Lorentz-Cauchy distribution function.

#221980 - $15.00 USD Received 1 Sep 2014; revised 25 Oct 2014; accepted 25 Oct 2014; published 31 Oct 2014

2.4 Cell culture and sample preparation

For experimental validation of SUPRA microscopy, we tested with mouse macrophage-like cell line of J774. J774 cells were cultured on metal films containing surface nanodot arrays for 24 h in RPMI 1640 medium supplemented with 10% fetal bovine serum, penicillin and streptomycin, and 2 mM L-glutamate in a 5% CO_2 humidified incubator. Metal films were incubated with 1% gelatin solution (Sigma, St. Louis, MO) for 5 min at room temperature to enhance biocompatibility and washed with RPMI 1640 medium. Cell viability was evaluated to confirm biocompatibility on silver film and nanodots by cell counting kit-8 assay (CCK-8, Sigma-Aldrich, St. Louis, USA), which determined the cell viability on nanodot array samples to be around ~86%. Although cell viability is reduced on silver nanodots compared to normal dish culture, it was sustainable within 24 hrs. For SEM, J774 cells were fixed with 2.5% glutaraldehyde overnight at 4°C and were subjected to critical point drying. To obtain cytoskeletal images of F-actin, cells were fixed with 4% paraformaldehyde and stained with 1 μM phalloidin-FITC (Sigma, St. Louis, MO), which is used to selectively stain F-actin and prevent its depolymerization by interfering between F-actin subunits and locking adjacent subunits together, for 30 min at room temperature.

3. Results and discussion

3.1 Numerical results

Despite the good biocompatibility and chemical stability of gold, we have used silver for nanodot arrays because of far superior plasmonic enhancement [37]. Figure 3(a) shows the evanescent wave intensity ($|E|^2$) distribution in 3D and 2D that is overlayed with the nanodot array patterns. Localization of electromagnetic fields on the silver nanodot arrays to form localized hot spots is clear, although it tends to be less localized near the edge of a block due to the SP propagation. Size analysis of the intensity profiles obtained from Fig. 3(a) was performed with ImageJ after defining the size of localized fields as the diameter at which intensity of the fields is twice as high as that of incident light when the localized field is assumed to be circularly symmetric. The results presented in Fig. 3(b) in terms of a size distribution histogram strongly suggest that the size should fall in the range of 100 - 150 nm. The histogram fits well with a Cauchy-Lorentzian distribution with center and width at 135 and 160 nm, respectively.

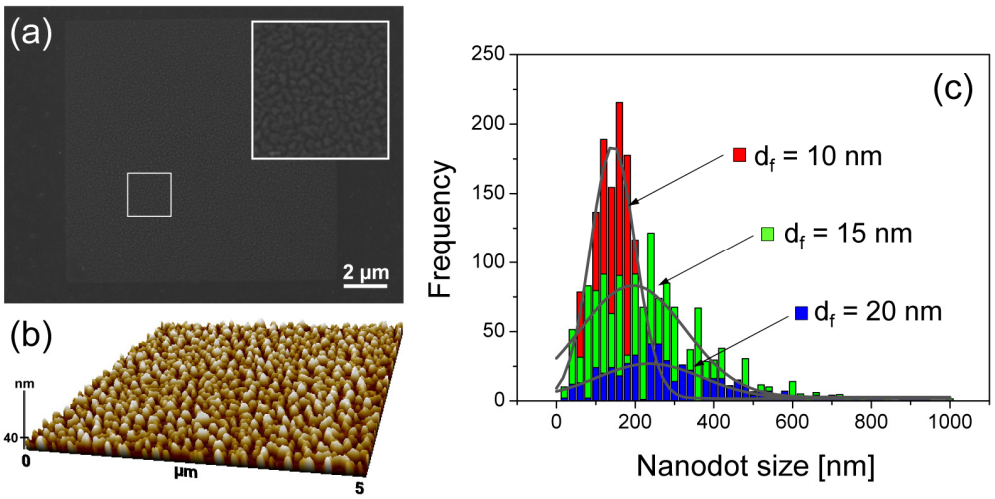

Fig. 4. (a) SEM images of blocked random nanodot array samples. Inset: magnified image of nanodot arrays shown as a square in an area of 2 × 2 μm^2. (b) AFM image of nanodots. (c) Size distribution of nanodot arrays.

#221980 - $15.00 USD Received 1 Sep 2014; revised 25 Oct 2014; accepted 25 Oct 2014; published 31 Oct 2014

3.2 Nanodot characteristics

Scanning electron microscope (SEM) and atomic force microscope (AFM) images of blocked nanodot array samples are shown in Figs. 4(a) and 4(b), respectively. The investigation of the distribution of nanodot size shown in Fig. 4(c) reveals that the average nanodot size increases with the silver-film thickness (d_f) used to synthesize the nanodots, almost linearly: at d_f = 10, 15 and 20 nm, average nanodot size was obtained as 143.4 ± 113.2, 194.0 ± 267.5, and 237.0 ± 267.2 nm (center ± width), respectively, when fit in a normal distribution as shown in Fig. 4(c), i.e., a 5-nm increase of silver enlarges nanodots by 46.8 nm on average. The correlation between the average nanodot size and d_f was strong with correlation coefficient R = 0.9978. Nanodots grow in size with the underlying silver film thickness as they become connected by dewetting [38]. Also observed (data not shown in Fig. 4) is that the separation varies less significantly from 25 to 75 nm as d_f changes between 10 and 20 nm. The nanodot characteristics were not significantly different from those obtained without blocks. Overall, the results indicate that the nanodot distributions may be controlled statistically by varying process parameters such as the film thickness and thus can be used to modify the characteristics of near-field localization.

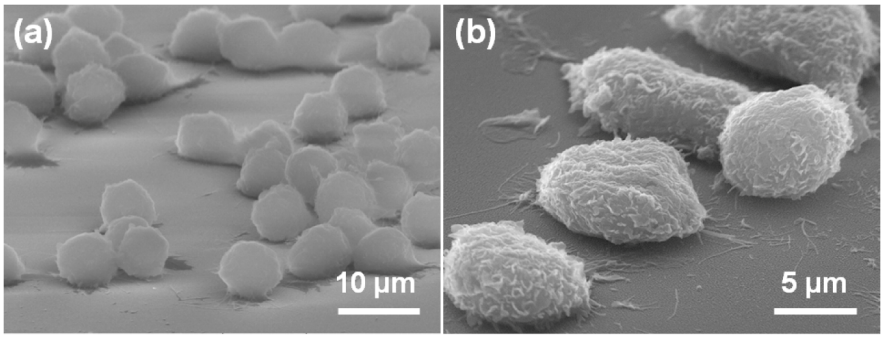

Fig. 5. SEM images of J774 cells on the substrates: (a) metal film and (b) random nanodot arrays. Overall, good adhesion of cultured cells was observed on all the substrates.

3.3 Raw Images of Intracellular Cytoskeletal Actin Filaments on Nanodot Arrays

Figure 5 shows a SEM image of J774 cells on the silver film and nanodot arrays. The images as well as cell viability tests described in Section 2.4 show overall good adhesion of cultured cells for both types of substrates. Interestingly, the improved cell viability was observed on nanodots, presumably associated with less contact between silver and cell membrane. Figure 6 presents raw images of J774 cells measured on the glass substrate (top row), silver film (middle row) and nanodot arrays (bottom row). Bright-field and epifluorescence images, respectively shown in Figs. 6(a) and 6(b), on the glass substrate, bare film, and nanodots describe general cell morphology and raw distribution of phalloidin. Figure 6(c) shows cell images measured by TIRF microscopy (TIRFM) on glass substrate and silver film and by SUPRA microscopy on the nanodot arrays, respectively. It is noticeable that image brightness is slightly reduced in the case of SUPRA microscopy because of reduced field intensity where fields are not localized. FITC-conjugated phalloidin molecules present the distribution of F-actin that is much smaller than the size of localized fields, which suggests that each fluorescent spot observed in Fig. 6 may not be produced from a single phalloidin molecule. The raw images acquired by SUPRA microscopy and TIRFM do not present significant differences in terms of intensity contrast. However, SUPRA microscopy allows super-resolved image reconstruction based on field localization, which is described in the next section.

#221980 - $15.00 USD Received 1 Sep 2014; revised 25 Oct 2014; accepted 25 Oct 2014; published 31 Oct 2014

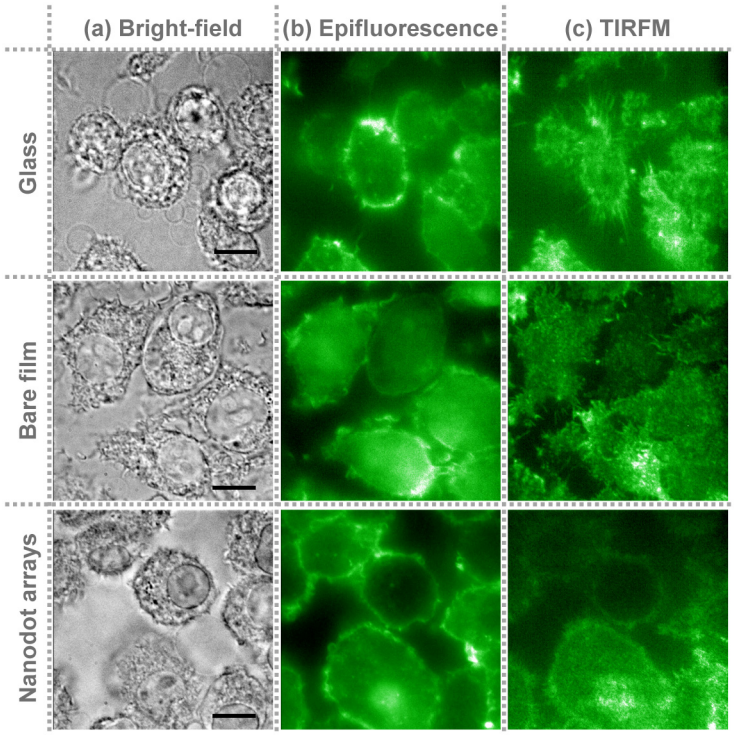

Fig. 6. Measured images of J774 cells on the glass substrate (top row), metal film (middle row) and nanodot arrays (bottom row): (a) bright-field, (b) epifluorescence, and (c) TIRFM images. Scale bar: 10 μm.

3.4 Image reconstruction

Image reconstruction beyond the diffraction limit can be performed by deconvolving the spatial distribution of detected phalloidin fluorescence assuming that the distribution of localized fields is known *a priori*. From the linear imaging theory, a far-field image $I(x,y)$ is related to the near-field distribution $f(\xi,\eta)$ which is calculated by RCWA as described in Section 2.2 or can be measured in the near-field. (x,y) and (ξ,η) represent 2D coordinates of image and object plane, as follows:

$$I(x,y)=\left[f(\xi,\eta)\,g(\xi,\eta)\right]\otimes h(x-\xi,y-\eta). \tag{1}$$

In Eq. (1), $h(\xi,\eta)$ is the PSF of the far-field optics. $g(\xi,\eta)$ denotes the molecular distribution under imaging and the molecular density of fluorescent probes is not assumed to limit the imaging characteristics. Despite the simplicity, Eq. (1) reveals the nature of SUPRA microscopy and how it achieves super-resolution, i.e., what is measured is the fluorescence image sampled by the localized near-fields and then convolved by the far-field PSF. Images can be reconstructed by the effective PSF that is much smaller than the diffraction limit associated with $f(\xi,\eta)$. Simple deconvolution based on Eq. (1) to obtain $g(\xi,\eta)$ is often quite difficult because the process is ill-posed and involves many operations of division by zero and amplification of noise that can lead to major artifacts [39]. For this reason, image reconstruction was performed based on estimation in which random fluorophore distributions are generated to match a measured image field probabilistically. The procedure relies on the field distribution as the stochastic probability of fluorescence excitation. After being weighted by near-fields, an optimum distribution that produces a far-field image closest to the measured image was found.

#221980 - $15.00 USD Received 1 Sep 2014; revised 25 Oct 2014; accepted 25 Oct 2014; published 31 Oct 2014

Our implementation of the deconvolution process starts with image resizing. An object located on the blocked nanodot arrays (12.2 × 12.2 μm^2 in size) is presented as a 115 × 115 pixel image when captured by CCD. Thus, a single pixel is approximately 106 × 106 nm^2, which may be too coarse to express an object. Therefore, an image was first enlarged to be of 510 × 510 pixels. The distribution of fluorescent dyes is assumed to be random. Then, the number of total fluorescent dyes was estimated so as to minimize the error ε, which is defined as an l_2 norm of image difference between $\hat{I}(x,y)$ and $I(x,y)$. Here, $\hat{I}(x,y)$ and $I(x,y)$ represent intermediate fluorescence image corresponding to an estimated molecular distribution $\hat{g}(\xi,\eta)$ and true intensity image. The relation can be expressed as

$$\hat{I}(x,y) = \left[f(\xi,\eta)\,\hat{g}(\xi,\eta) \right] \otimes h(x-\xi, y-\eta) \tag{2}$$

$$\varepsilon = \sqrt{\sum_{x,y} \left[I(x,y) - \hat{I}(x,y) \right]^2} \tag{3}$$

Once the number of fluorescent dyes with a minimum l_2 norm is found in range, estimated $\hat{I}(x,y)$ is calculated repetitively which corresponds to random dye distribution $\hat{g}(\xi,\eta)$ so that the l_2 norm is further minimized to find $\hat{g}(\xi,\eta) \approx g(\xi,\eta)$. This process may be simplified mathematically as follows:

$$\arg\min_{\hat{g}(\xi,\mu)} \varepsilon = \left\{ \hat{g}(\xi,\mu) \mid \varepsilon = \sqrt{\sum_{x,y} \left[I(x,y) - \hat{I}(x,y) \right]^2}, \text{when} \sum_{\xi,\eta} \hat{g}(\xi,\mu) = N \right\} \tag{4}$$

which is similar in concept to an earlier study, although specific implementation of the algorithm is different [40].

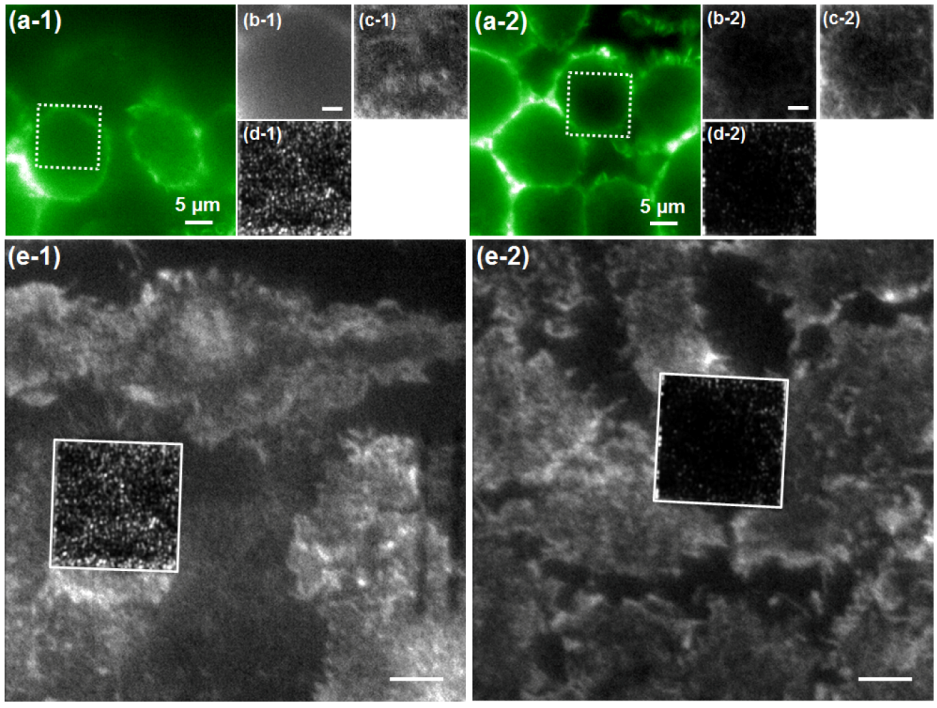

Fig. 7. Epifluorescence and SUPRA images of cells after reconstruction measured at two different sample points (1,2). (a) Epifluorescence image: the squares represent a nanodot block. Magnified images are in (b-d): (b) epifluorescence, (c) raw data, and (d) SUPRA after reconstruction. Scale bar: 2 μm. For (e), reconstructed SUPRA images were used in place of raw images. Scale bar: 5 μm.

#221980 - $15.00 USD Received 1 Sep 2014; revised 25 Oct 2014; accepted 25 Oct 2014; published 31 Oct 2014

Figure 7 shows the images of two different cells before and after reconstruction where image areas outside the reconstructed block correspond to measured raw data. The dashed square represents a block of random nanodot arrays in a size of 12.2 × 12.2 μm^2. Epifluorescence images show blurred plasma membrane F-actin [Figs. 7(a) and 7(b)] and it is difficult to identify cytoplasmic F-actin at two different points. However, after raw images of Fig. 7(c) are reconstructed, SUPRA images of cells show F-actin in resting state of J774 cells, which present actin cytoskeleton with minimally polarized and diffusely organized active filaments [Figs. 7(d) and 7(e)]. For comparison of the images on nanodot arrays, control experiments were performed with fluorescent nanobeads on plasmonic nanodots without cells (not shown) and the disparity of the control images show that the image presented in Figs. 7(d) and 7(e) is not just the network of random plasmonic field localization, but clearly reflects the structure of actin cytoskelenton. Whole cell images of Fig. 7(e) emphasize the enhancement of image resolution. Because the enhancement is achieved by the field localization due to metallic random nanodot arrays, the resolution is strongly dependent on the size of localized fields and thus is not spatially constant. In agreement with the size of localized fields, the resolution is estimated to be in the range of 100-150 nm, i.e., molecules that are apart from each other by this distance can be resolved. In this sense, the size should be one of the main factors that determine the accuracy of SUPRA microscopy and stronger field localization is in general desired to produce a smaller field. From the signal processing standpoint, the reconstruction presented in Figs. 7(d) and 7(e) represents an image of cytoskeletal actin filament that is sampled by the pseudorandom arrays of hot spots created by nanodots.

The effectiveness of SUPRA microscopy depends on the distribution of localized fields, target concentration (i.e., concentration of molecules that fluorescent dyes target and bind to), and more explicitly the size of target molecules relative to the localized fields. If localized fields are dense to a degree that multiple hot spots are captured by an imaging pixel in the far-field, the fluorescence excited by these hot spots cannot be resolved. The distribution of localized fields shown in Fig. 4 suggests that this should not be the case and that an imaging pixel may not have more than one localized field.

The way that SUPRA microscopy is affected by target concentration is related to the sparseness of field localization, i.e., imaging performed at localized fields prefers target concentration that is much higher than the distribution of localized fields. In regard to the size, SUPRA is effective for single target imaging if the target is approximately equal in size to the spatial scale of localized fields. In this study, FITC-conjugated phalloidin is much smaller than the localized fields. This sets the limit on the number of phalloidin molecules that SUPRA microscopy can be used to detect.

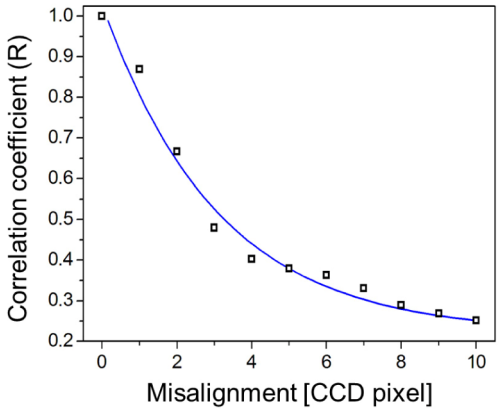

Fig. 8. Correlation coefficient between the reconstructed far-field image with perfect alignment and one reconstructed with displacement from the near-field distribution in terms of CCD pixels.

#221980 - $15.00 USD Received 1 Sep 2014; revised 25 Oct 2014; accepted 25 Oct 2014; published 31 Oct 2014

3.5 Effect of misregistration

Note also that SUPRA microscopy, since it acquires data in the far-field, presumes perfect alignment between near-field distribution and far-field images. Misalignment may occur within the diffraction limit, which affects the near-field distribution used for the image reconstruction and can ultimately change reconstructed images. Figure 8 presents the correlation coefficient R between the reconstructed far-field image with perfect alignment [Fig. 7(d)] and one reconstructed after displacement from the near-field distribution in terms of CCD pixels. For the calculation of R, the correlation coefficient was taken while an image is displaced linearly along the left direction of the near-field. It is clear that the correlation decreases monotonically with misalignment: misalignment by one CCD pixel results in R = 86%, which eventually floors near 25%.

Maximum misalignment that may be incurred in the reconstruction process is estimated to be on the order of one CCD pixel. The reconstructed images assuming the registration corresponding to the misalignment in the lateral plane are presented in Fig. 9. The results confirm that the correlation between reconstructed images remain very high with correlation coefficient R exceeding 81%, regardless of the direction that the registration takes place. Under the fixed misalignment, the correlation is degraded as the image resolution improves, because image reconstruction becomes more sensitive to the misalignment. Overall, the results presented in Figs. 8 and 9 suggest the effect of far-field registration to be negligible in the course of image reconstruction.

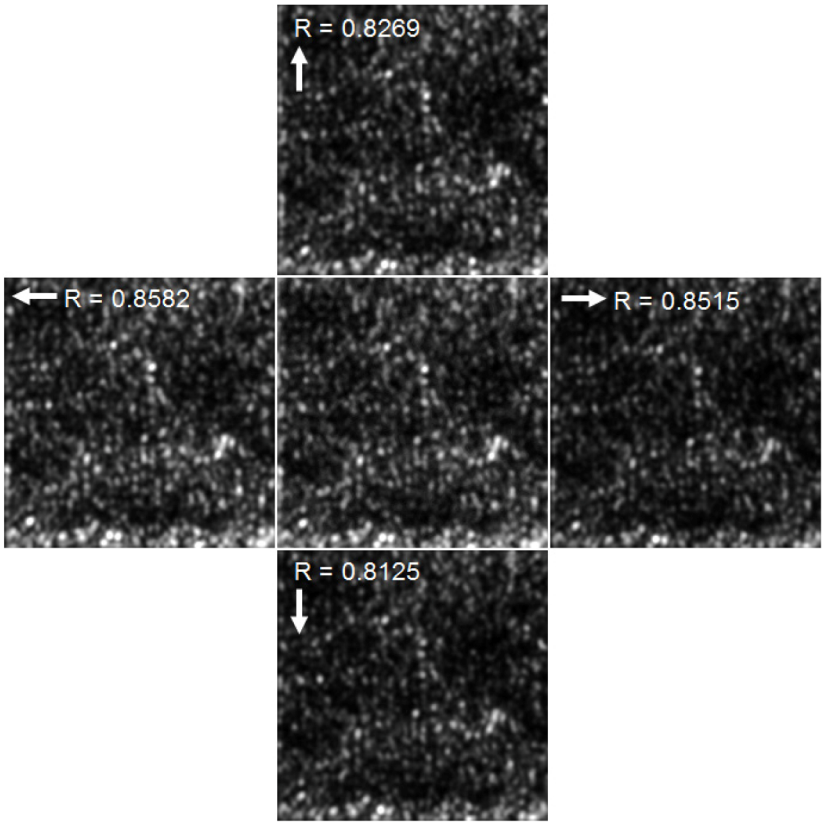

Fig. 9. Effects of registration in the lateral plane on the image reconstruction: reconstructed image for perfect registration (no misalignment) at the center and images reconstructed with misalignment by one CCD pixel in the right, left, top, and bottom direction (direction shown as arrow). Correlation coefficient R is shown to remain higher than 81% regardless of the way that the registration takes place.

#221980 - $15.00 USD Received 1 Sep 2014; revised 25 Oct 2014; accepted 25 Oct 2014; published 31 Oct 2014

4. Concluding remarks

In conclusion, we have investigated the feasibility of super-resolution microscopy with silver nanodot arrays. The concept was experimentally validated for visualizing intracellular actin filaments. The image resolution is mainly determined by the size of localized fields in the range of 100-150 nm. The biggest advantage of SUPRA microscopy lies in the ease of synthesis and wide availability of random nanopatterns to achieve super-resolution. Also, the patterns can be synthesized to vary the degree of randomness and thus the imaging characteristics. Further enhancement of image resolution may be feasible, for example, by combining SUPRA microscopy with switching of localized fields by a known distance.

Acknowledgment

This work was supported by the National Research Foundation (NRF) grants funded by the Korean Government [MSIP] (2011-0017500, 2011-0017611, and NRF-2012R1A4A1029061).

#221980 - $15.00 USD Received 1 Sep 2014; revised 25 Oct 2014; accepted 25 Oct 2014; published 31 Oct 2014